Supporting Information

Precursor degree of polymerization engineering to understand the sodium storage behavior of closed pores in hard carbon

Haojie Du [a, b] , Lu Zhou [a, b], Rucan Chen [a, b], Lei Zhang [a, b,*], Xueyi Guo [a, b], Qinghua Tian [a, b], Qinmeng Wang [a, b,], Hui Tong [a, b], and Shuo Wang [c]**

a School of Metallurgy and Environment, Central South University, Changsha 410083, China.

b Cleaner Metallurgical Engineering Research Center, China Nonferrous Metals Industry Association, Changsha 410083, China.

c BTR New Material Group Co. , Ltd. Shenzhen 518107, China.

* *Correspondence to: Lei Zhang, No. 932 Lushan southe road, Changsha, Hunan province, 410083, People's Republic of China, E-mail: zhang_lei@csu.edu.cn, telephone: +8615111172871.*

** *Correspondence to: Qinmeng Wang, No. 932 Lushan southe road, Changsha, Hunan province, 410083, People's Republic of China, E-mail: qm_wang@163.com, telephone: +8613574812541.*

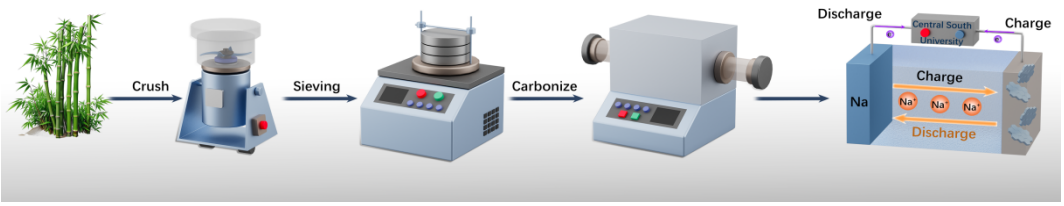

Fig. S1 Schematic illustration of the synthesis procedure

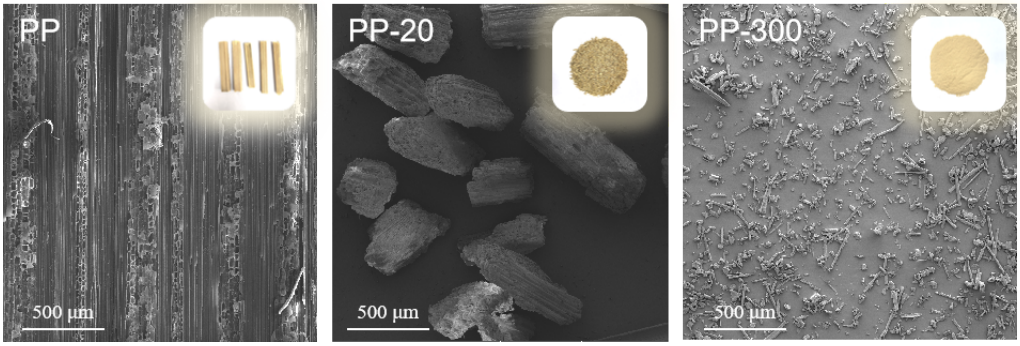

Fig. S2 SEM images of PP, PP-20, and PP-300

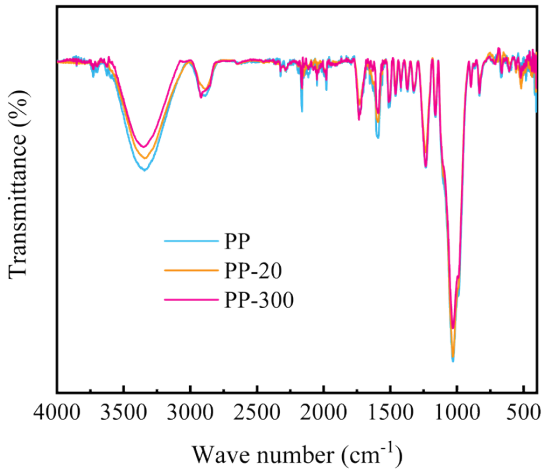

Figure S3. Baseline-corrected FTIR curves of PP, PP-20, and PP-300.

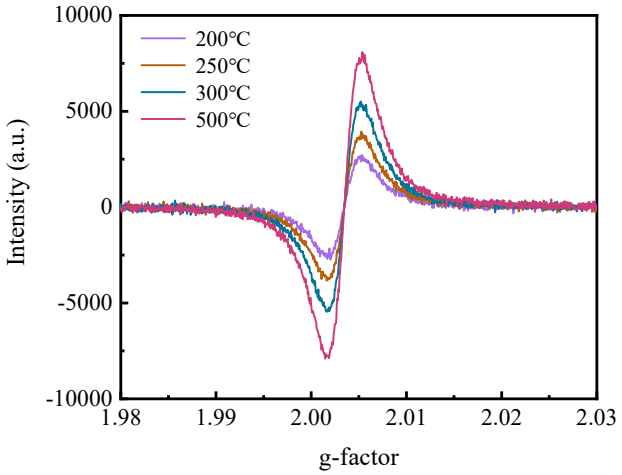

Figure S4. g-factor of PP at different temperatures

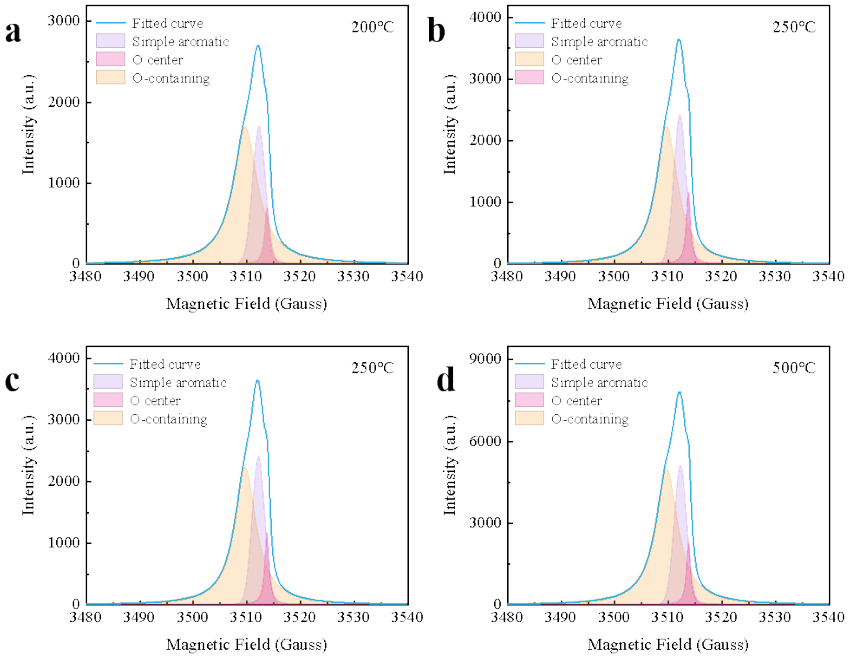

Figure S5. EPR Fitted curves of PP at different temperatures

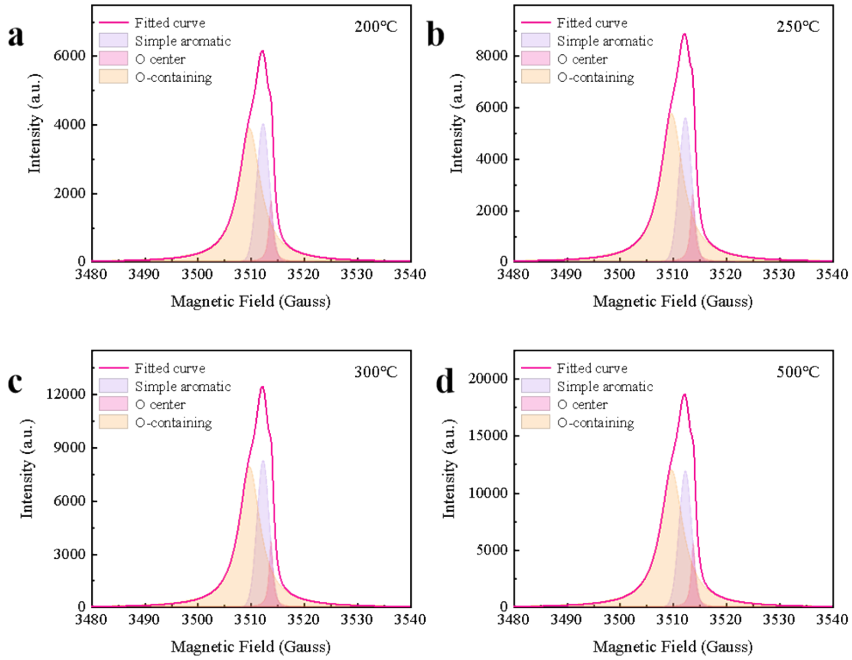

Figure S6. EPR fitted curves of PP-300 at different temperatures

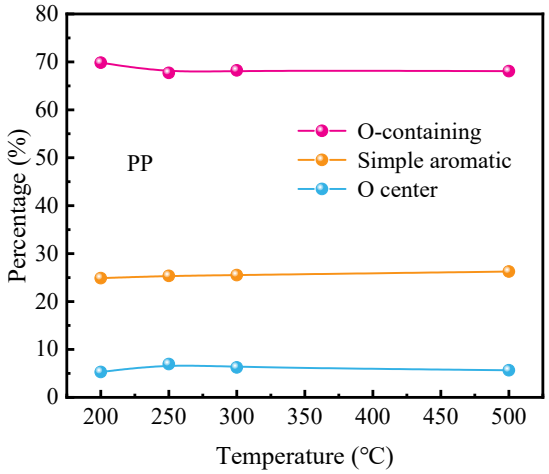

Figure S7. Percentage of free radicals of PP at different temperatures

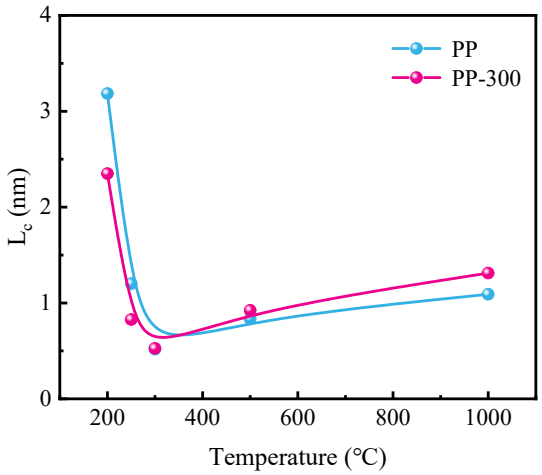

Figure S8. Lc of PP and PP-300 at different temperatures

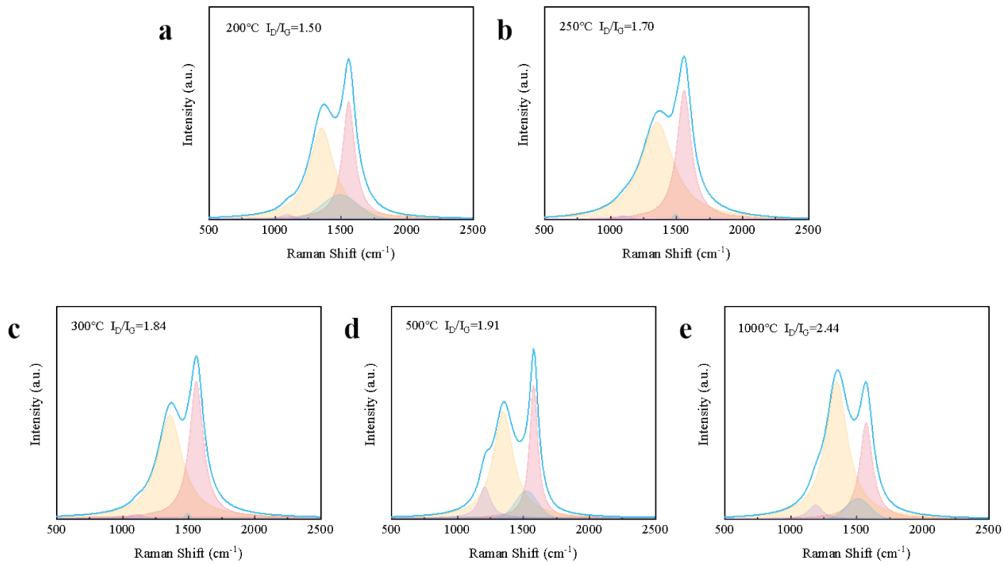

Figure S9. Raman fitted curves of PP at different temperatures

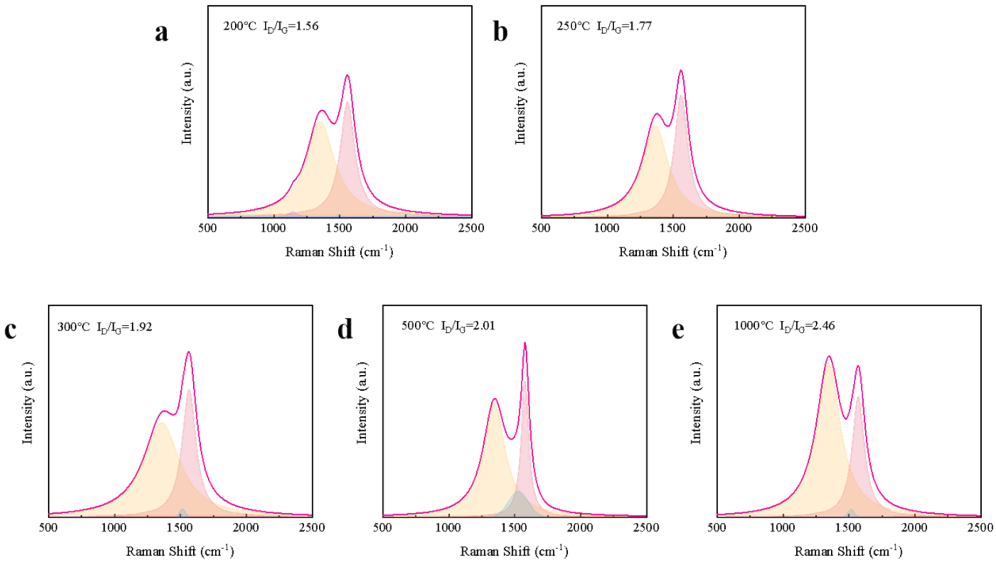

Figure S10. Raman fitted curves of PP-300 at different temperatures

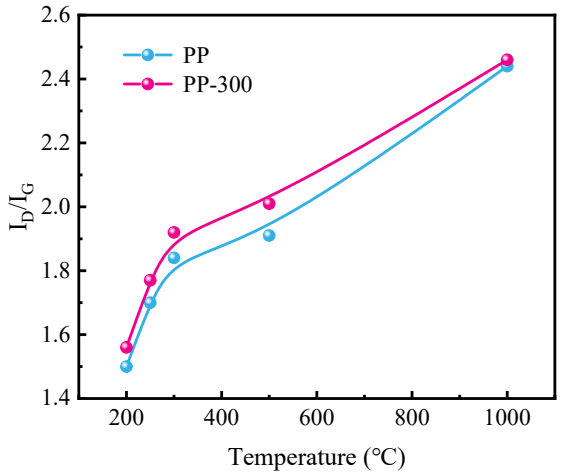

Figure S11. I_D/I_G of PP and PP-300 at different temperatures

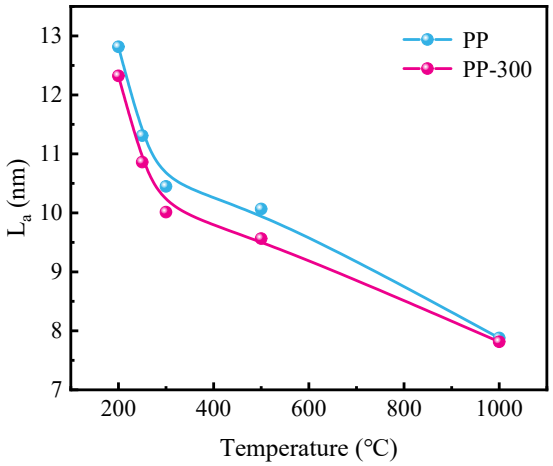

Figure S12. La of PP and PP-300 at different temperatures

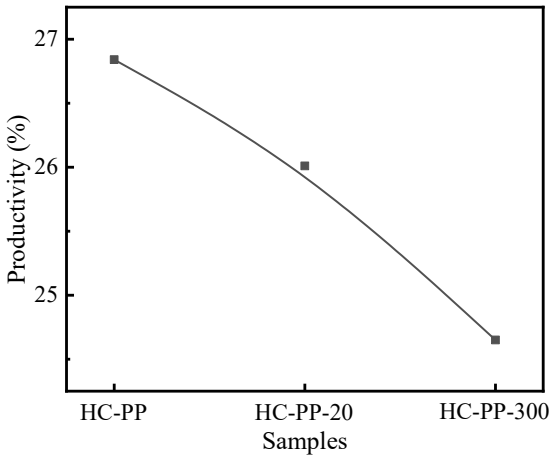

Figure S13. Carbonization yield of PP, PP-20, and PP-300

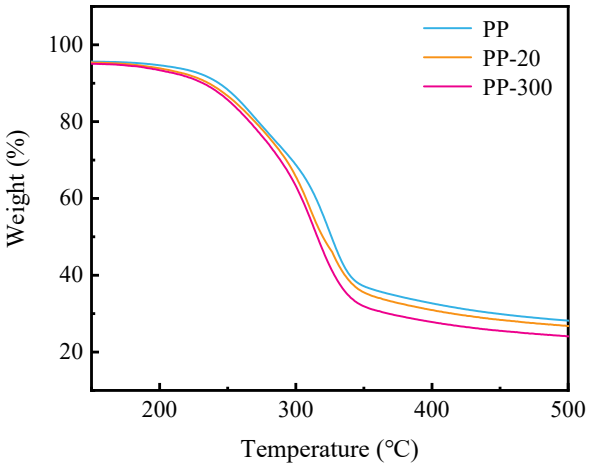

Figure S14. Thermogravimetric analysis curves of PPs

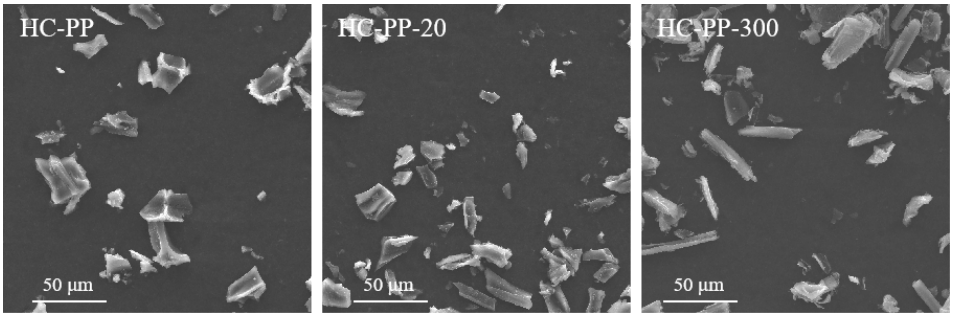

Figure S15. SEM images of of HC-PP, HC-PP-20, and HC-PP-300

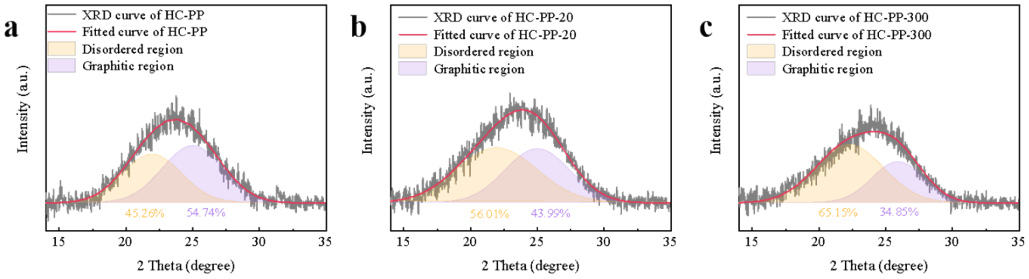

Figure S16. XRD fitted curves of HC-PP, HC-PP-20, and HC-PP-300

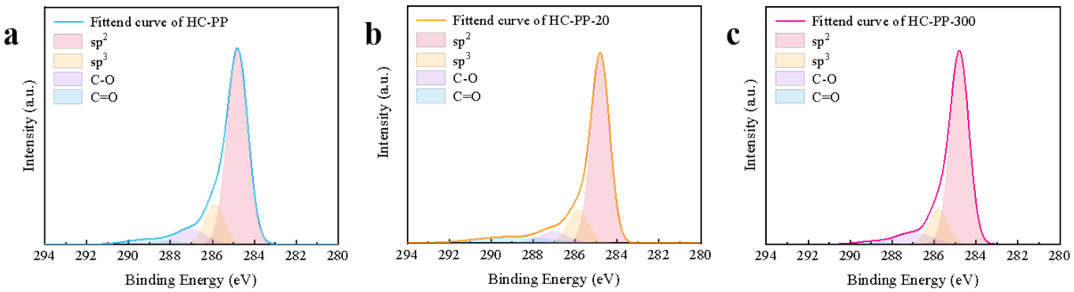

Figure S17. XPS C1s spectra and fitted curves of HC-PP, HC-PP-20, and HC-PP-300

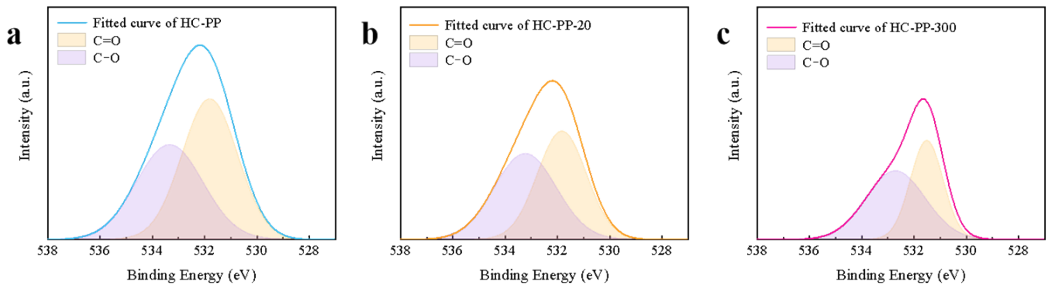

Figure S18. XPS O1s spectra and fitted curves of HC-PP, HC-PP-20, and HC-PP-300

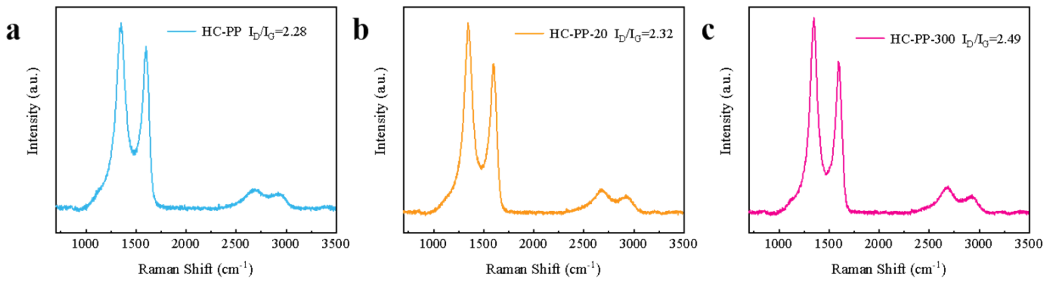

Figure S19. Raman curves of HC-PP, HC-PP-20, and HC-PP-300

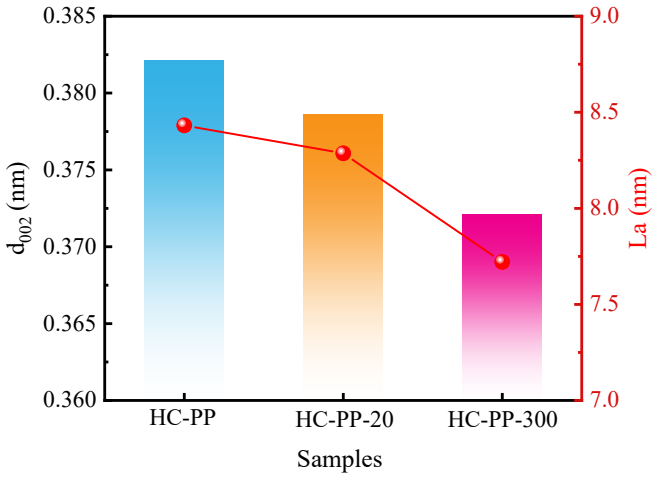

Figure S20. d002 and La of HC-PP, HC-PP-20, and HC-PP-300

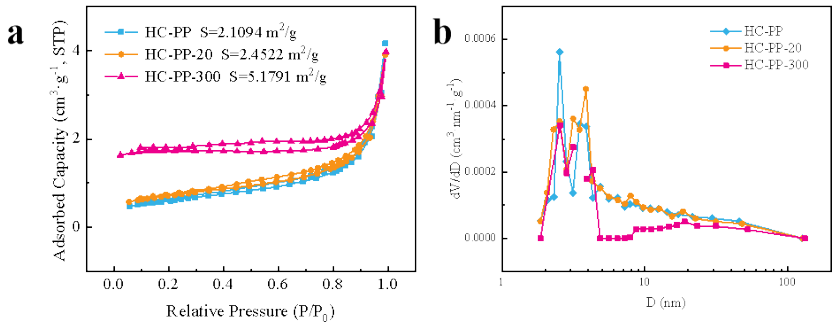

Figure S21. Nitrogen adsorption and desorption isothermal curves and pore size distribution of HC-PP, HC-PP-20, and HC-PP-300

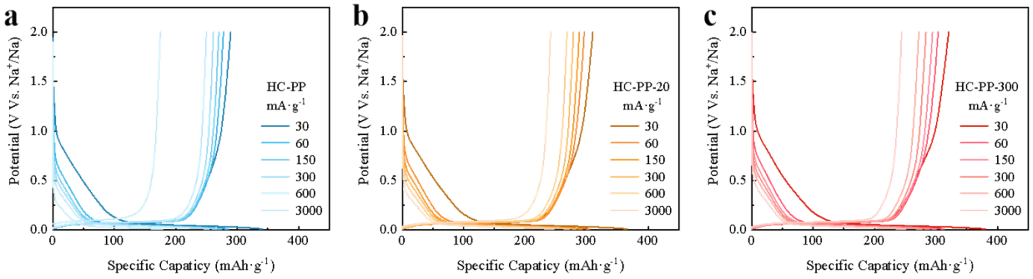

Figure S22. The GCD curves at different current densities of HC-PP, HC-PP-20, and HC-PP-300

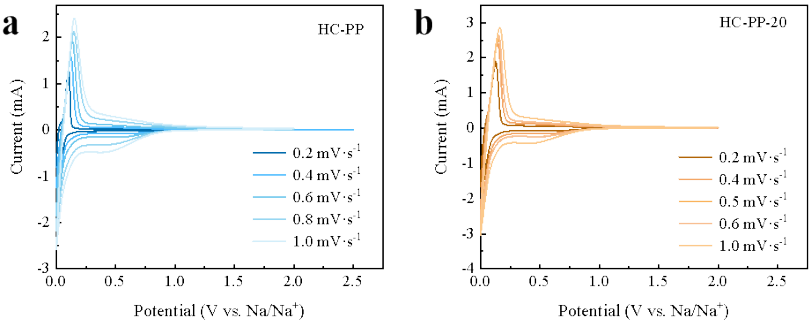

Figure S23. CV curves of HC-PP(a), HC-PP-20(b) at various scan rates of 0.2, 0.4, 0.6, 0.8, 1.0 mV s^{-1}.

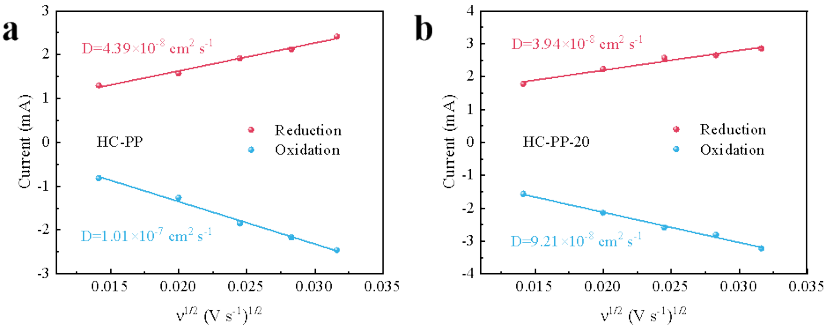

Figure S24. Na^+ diffusion coefficient of HC-PP(a), HC-PP-20(b) at various scan rates of 0.2, 0.4, 0.6, 0.8, 1.0 mV s^{-1}.

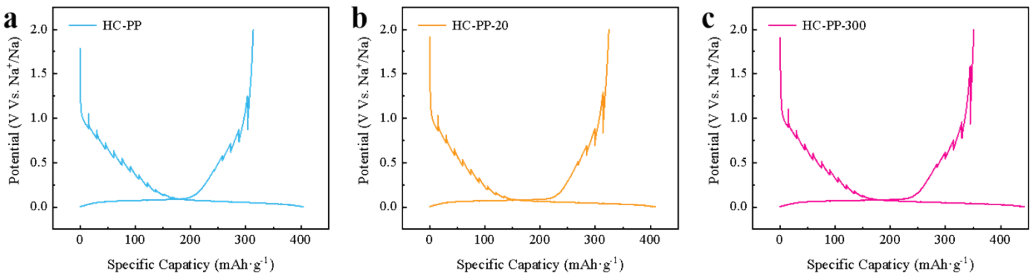

Figure S25. GITT curves of HC-PP, HC-PP-20, and HC-PP-300

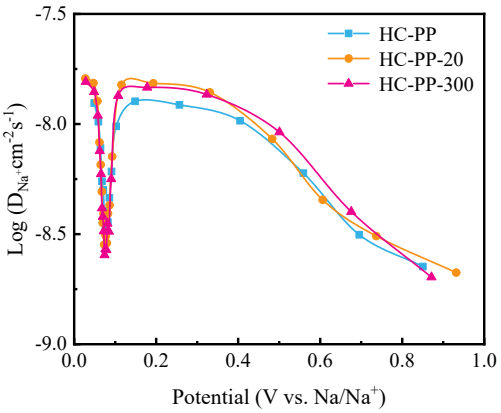

Figure S26. Na^+ diffusion coefficient of HC-PP, HC-PP-20, HC-PP-300 calculated from GITT during charge process

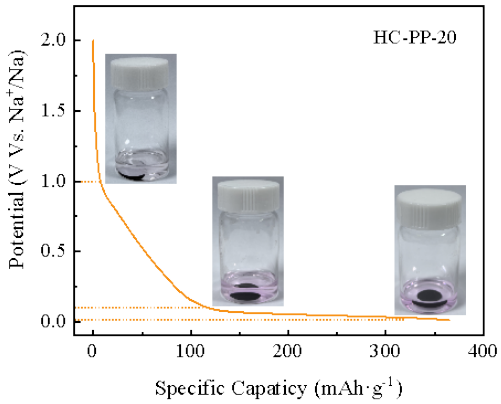

Figure S27. The color change of ethanol solution containing 1% phenolphthalein after reaction with HC-PP-20 electrode.

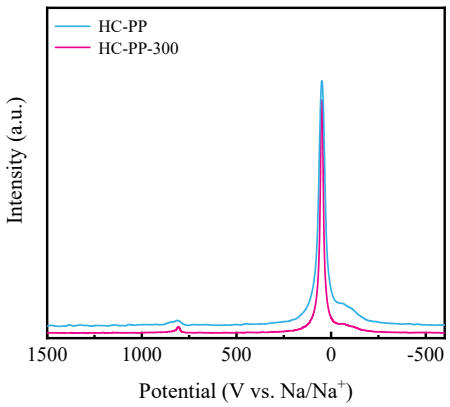

Figure S28. Sodium NMR patterns of HC-PP, and HC-PP-300 after discharging to 0.01V

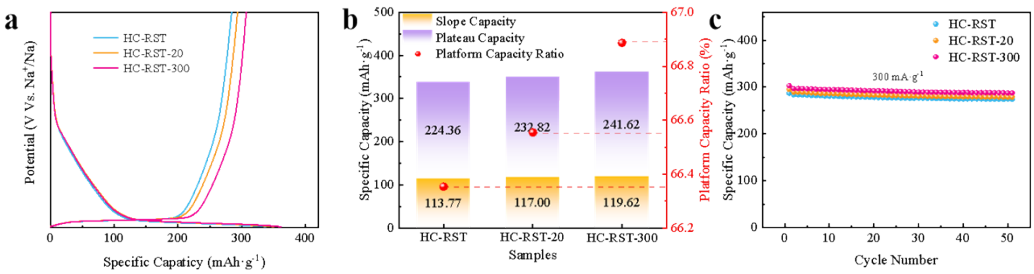

Figure S29. a) The GCD curves of HC-RST, HC-RST-20, and HC-RST-300 at 30 mA g^{-1}. b) The capacity ratios of slope capacity (>0.1 V) and plateau capacity (<0.1 V) of HC-RST, HC-RST-20, and HC-RST-300. c) The cycling performance of HC-RST, HC-RST-20, and HC-RST-300 at 300 mA g^{-1}.

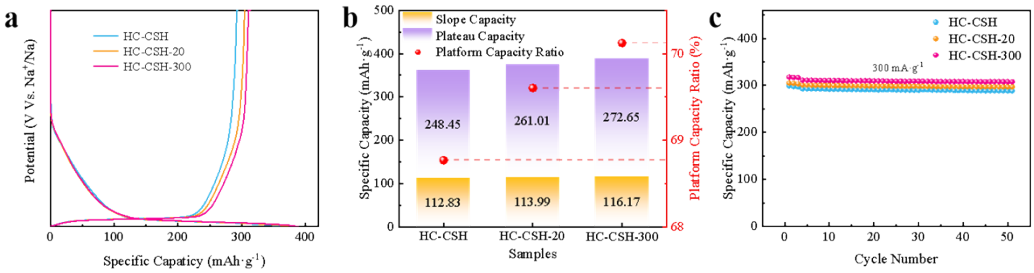

Figure S30. a) The GCD curves of HC-CSH, HC-CSH-20, and HC-CSH-300 at 30 mA g^{-1}. b) The capacity ratios of slope capacity (>0.1 V) and plateau capacity (<0.1 V) of HC-CSH, HC-CSH-20, and HC-CSH-300. c) The cycling performance of HC-CSH, HC-CSH-20, and HC-CSH-300 at 300 mA g^{-1}.

Table S1. The composition of phyllostachys pubescens

Composition	Cellulose	Lignin	Hemicellulose	Others
Content	36.1%	28.1%	15.1%	20.7%

Table S2. Structure parameters of PP, PP-20, PP-300.

Samples	L_c	*CrI*	*Mw*	*Mp*	Carbon yield at 1500℃
Units	nm	%	g mol^{-1}	g mol^{-1}	%
PP	2.88	61.69	172575	324126	26.84
PP-20	2.84	49.72	151463	273057	26.01
PP-300	2.72	47.80	121139	147887	24.65

Table S3. Structure parameters of HC-PP, HC-PP-20, HC-PP-300.

Samples	d_{002}	L_c	I_D/I_G	$L_{a,\ Raman}$	$S_{BET}(N_2)$	D_{BET}	V_{BET}	True density	V_{Closed}
Units	nm	nm	-	nm	m^2 g^{-1}	nm	cm^3 g^{-1}	g cm^{-3}	cm^3 g^{-1}
HC-PP	0.382	1.15	2.28	8.43	2.11	11.47	0.0063	2.0610	0.0427
HC-PP-20	0.379	1.06	2.32	8.29	2.45	9.79	0.0060	1.6821	0.1520
HC-PP-300	0.372	1.01	2.49	7.72	5.18	4.48	0.0058	1.5643	0.1968

Table S4. Electrochemical performance of HC-PP, HC-PP-20, HC-PP-300.

Samples	*ICE*	Specific capacity	Plateau capacity	Plateau capacity ratio	D_{Na+}
Units	%	mAh g^{-1}	mAh g^{-1}	%	cm^2 s^{-1}
HC-PP	84.37	293.64	231.19	66.43	1.01 * 10^{-7}
HC-PP-20	85.96	313.48	251.88	69.03	9.21 * 10^{-8}
HC-PP-300	85.58	327.06	268.98	70.38	8.83 * 10^{-8}

Table S5. Electrochemical performance of HC-WS, HC-WS-20, HC-WS-300.

Samples	*ICE*	Specific capacity	Plateau capacity	Plateau capacity ratio
Units	%	mAh g^{-1}	mAh g^{-1}	%
HC-WS	78.04	281.58	246.06	67.02
HC-WS-20	78.98	302.68	257.88	67.87
HC-WS-300	80.31	317.64	273.61	68.64

Table S6. Electrochemical performance of HC-CS, HC-CS-20, HC-CS-300.

Samples	*ICE*	Specific capacity	Plateau capacity	Plateau capacity ratio
Units	%	mAh g^{-1}	mAh g^{-1}	%
HC-CS	81.39	294.04	248.45	68.77

HC-CS-20	81.38	305.16	261.01	69.60
HC-CS-300	80.67	313.65	272.65	70.12

References for this supporting information

1. L. Ma *et al.*, Effect of alkali and alkali earth metals on reactions of stable free radicals during biomass pyrolysis: an in-situ EPR study. *Fuel Processing Technology* **250**, (2023).
2. D. Bi, M. Yin, F. Huang, J. Zhang, W. Yi, Evolution and prediction model of environmentally-persistent free radicals in biomass three-component pyrolytic carbon with pyrolysis temperature. *Industrial Crops and Products* **206**, 117643 (2023).
3. Q. Peng *et al.*, Tailoring lignin-derived porous carbon toward high-energy lithium-ion capacitor through varying Sp2- and Sp3-hybridized bonding. *Advanced Functional Materials* **33**, 2308284 (2023).
4. X. Lei *et al.*, Regulation of composition, microstructure, and pore structure of biomass-based hard carbon to boost the sodium storage performance. *Journal of Energy Storage* **101**, (2024).
5. Z. Tang *et al.*, Revealing the closed pore formation of waste wood-derived hard carbon for advanced sodium-ion battery. *NATURE COMMUNICATIONS* **14**, 6024 (2023).
6. S. Zhou *et al.*, Regulating closed pore structure enables significantly improved sodium storage for hard carbon pyrolyzing at relatively low temperature. *SUSMAT* **2**, 357-367 (2022).
7. C. Nita, B. Zhang, J. Dentzer, C. Matei Ghimbeu, Hard carbon derived from coconut shells, walnut shells, and corn silk biomass waste exhibiting high capacity for Na-ion batteries. *Journal of Energy Chemistry* **58**, 207-218 (2021).